The effects of substitutional Fe-doping on magnetism in MoS$_2$ and WS$_2$ monolayers

Kyungnam Kang[1], **Shichen Fu**[1], **Kamran Shayan**[2] ⓘ, **Yoshimura Anthony**[3],
Siamak Dadras[2] ⓘ, **Xiong Yuzan**[4,5], **Fujisawa Kazunori**[6],
Mauricio Terrones[6,7], **Wei Zhang**[5], **Stefan Strauf**[8,9], **Vincent Meunier**[3] ⓘ,
A Nick Vamivakas[2,10,11] and **Eui-Hyeok Yang**[1,9] ⓘ

[1] Department of Mechanical Engineering, Stevens Institute of Technology, Hoboken, NJ 07030, United States of America
[2] The Institute of Optics, University of Rochester, Rochester, NY 14627, United States of America
[3] Department of Physics, Applied Physics, and Astronomy, Rensselaer Polytechnic Institute, Troy, NY 12180, United States of America
[4] Department of Electrical and Computer Engineering, Oakland University, Rochester, MI 48309, United States of America
[5] Department of Physics, Oakland University, Rochester, MI 48309, United States of America
[6] Department of Physics and Center for 2-Dimensional and Layered Materials, Pennsylvania State University, University Park, PA 16802, United States of America
[7] Department of Chemistry and Materials Science & Engineering, Pennsylvania State University, University Park, PA 16802, United States of America
[8] Department of Physics, Stevens Institute of Technology, Hoboken, NJ 07030, United States of America
[9] Center for Quantum Science and Engineering, Stevens Institute of Technology, Hoboken, NJ 07030, United States of America
[10] Department of Physics, University of Rochester, Rochester, NY 14627, United States of America
[11] Center for Coherence and Quantum Optics, University of Rochester, Rochester, NY 14627, United States of America

E-mail: eyang@stevens.edu

CrossMark

Abstract

Doping of two-dimensional (2D) semiconductors has been intensively studied toward modulating their electrical, optical, and magnetic properties. While ferromagnetic 2D semiconductors hold promise for future spintronics and valleytronics, the origin of ferromagnetism in 2D materials remains unclear. Here, we show that substitutional Fe-doping of MoS$_2$ and WS$_2$ monolayers induce different magnetic properties. The Fe-doped monolayers are directly synthesized via chemical vapor deposition. In both cases, Fe substitutional doping is successfully achieved, as confirmed using scanning transmission electron microscopy. While both Fe:MoS$_2$ and Fe:WS$_2$ show PL quenching and n-type doping, Fe dopants in WS$_2$ monolayers are found to assume deep-level trap states, in contrast to the case of Fe:MoS$_2$, where the states are found to be shallow. Using μm- and mm-precision local NV$^-$ magnetometry and superconducting quantum interference device, we discover that, unlike MoS$_2$ monolayers, WS$_2$ monolayers do not show a magnetic phase transition to ferromagnetism upon Fe-doping. The absence of ferromagnetism in Fe:WS$_2$ is corroborated using density functional theory calculations.

Supplementary material for this article is available online

(Some figures may appear in colour only in the online journal)

1

1. Introduction

Spin-based technologies have emerged as a viable path to overcome the increasing challenges of conventional CMOS transistor scaling. The materials for spintronics are expected to show ferromagnetism in semiconductors, air-stability, and a Curie temperature at or above room temperature (RT). The first generation of such materials has been realized by doping transition metals in conventional semiconductors known as a dilute magnetic semiconductor (DMS). Since the observation of ferromagnetism in p-type (In,Mn)As and (Ga,Mn)As at cryogenic temperature, realizing RT ferromagnetism in semiconductors has been a pursuit for a few decades to realize practical applications [1, 2]. While the RT ferromagnetism has been hypothesized in nitrides and oxides, such as (Ga, Mn)N and (Zn,Mn)O [3, 4], it has neither been confirmed broadly nor demonstrated for a device structure [5]. The highest recorded Curie temperature in bulk DMS crystals is still widely considered as 110 K in (Ga,Mn)As [6], showing the limitations of conventional DMS materials for practical spintronics device applications.

Recent excitement in the field of two-dimensional (2D) materials has demonstrated ferromagnetism in atomically thin layers of chromium-based and iron-based alloys such as chromium triiodide (CrI_3) [7], chromium tribromide ($CrBr_3$) [8], chromium germanium telluride ($Cr_2Ge_2Te_6$) [9], and iron germanium telluride (Fe_3GeTe_2) [10]. While these findings indicate the possibility of realizing magnetism in a 2D limit, those 2D ferromagnets remain either metallic or insulating [7, 11, 12]. Several theoretical studies have predicted that DMS based on transition metal dichalcogenide (TMD) monolayers would exhibit ferromagnetic behaviors even at RT, which is a critical requirement for practical applications. Fan *et al* used first-principles calculations to define the magnetic properties of MoS_2, showing that doping of V, Mn, Fe, Co, and Cu into MoS_2 monolayers with low concentration could yield DMSs [13]. Mishra *et al* reported long-range ferromagnetism in Mn-doped MoS_2, $MoSe_2$, $MoTe_2$, and WS_2 monolayers using density functional theory (DFT) [14]. Lin *et al* used first-principles calculations to show the magnetic properties in Fe, Co, and Mn-doped MoS_2 monolayers [15]. Experiential observations of magnetism have been made in bulk TMDs [16] or transition metal-doped few-layer TMDs, using dopants, including V [17], Mn [18], Co [19–21], Ni [21, 22], Cu [23], Nb [20] and Re [24]. RT ferromagnetism was shown in 5% Cu-doped MoS_2 nanosheets [23], 10% Co-doped MoS_2 nanocrystals [21] and 10% Ni-doped nanocrystals [21]. Recently, the RT ferromagnetism was successfully demonstrated in *in situ* Fe-doped MoS_2 (Fe:MoS_2) and V-doped WSe_2 (V:WSe_2) via chemical vapor deposition [25, 26]. However, the origin of ferromagnetism in such materials remains uncertain.

Here, we report the effects of Fe-doping on the magnetism in WS_2 monolayers by studying their optical, electrical, and magnetic properties of *in situ* synthesized Fe:WS_2 monolayers, and comparing with the case of Fe:MoS_2. We confirm the substitutional doping of Fe atoms into transition metal sites using the high-resolution scanning transmission electron microscopy (STEM). We show that Fe dopants produce two different trap states in Fe:MoS_2 and Fe:WS_2 by studying their photoluminescence signatures. Employing nitrogen-vacancy (NV$^-$) center magnetometry, and magnetization measurements using a superconducting quantum interference device (SQUID), we find that ferromagnetism appears only in Fe:MoS_2 monolayers, while Fe:WS_2 monolayers show a paramagnetic response. Using DFT calculations, we show that the magnetic properties in Fe:MoS_2 and Fe:WS_2 monolayers arise from the charge transfer between the Fe dopants and neighboring S atoms, and the magnetic moments of paired Fe atoms vanish only in Fe:WS_2.

2. Methods

2.1. Synthesis of Fe:WS$_2$ and Fe:MoS$_2$

The synthesis procedures of Fe:WS_2 and Fe:MoS_2 monolayers are shown in figure 1. Thin-film of transition metal oxide (WO_3 and MoO_3, Kurt J. Lesker, 99.99%) (5 nm thick) was deposited on a SiO_2/Si substrate prepared as the transition metal source. Iron oxide (Fe_3O_4, Alpha Chemicals) and sulfur powder (Alfa Aesar, 99.5%) were used for Fe and S sources, respectively. For the growth of Fe:WS_2 monolayers, a Fe_3O_4 powder (0.01 g) was sandwiched between a bare SiO_2/Si substrate and the WO_3-deposited SiO_2/Si substrate. The prepared substrate was loaded in the middle of the furnace tube. A sulfur powder (0.6 g) was loaded upstream. After loading the substrates and precursors, Ar gas (Praxair, UHP) was supplied while the mechanical pump was running to purge ambient air. The base and growth pressures were 150 mTorr and 3 Torr, respectively. Then the furnace temperature was increased up to 900 °C, which was held for 5 min. After completing the growth, the furnace lid was opened to cool down the sample to RT before the samples were taken out. The growth recipe of Fe:MoS_2 monolayers was similar to that of Fe:WS_2 monolayers, except for using MoO_3 instead of WO_3. The growth process of undoped WS_2 monolayers was also similar to that of the growth process of Fe:WS_2 monolayers, except for its growth without Fe_3O_4.

2.2. Characterization of Fe:MoS$_2$ and Fe:WS$_2$

STEM was carried out on an FEI Titan^3 G2 S/TEM operated at 80 kV to investigate the atomic structure of WS_2 and MoS_2 triangles. A high-angle annular dark-field (HAADF) detector was used for Z contrast imaging. To reduce noise and increase the visibility of atoms, a Gaussian Blur filter with a blurring width of 0.03 nm was applied with an image processing program called ImageJ.

Raman and RT PL spectroscopies were performed using a Horiba XPLORA spectrometer equipped with a 532 nm laser at the atmospheric pressure. Low-temperature micro-photoluminescence (μ-PL) measurements were taken inside a closed-cycle cryostat (attoDRY1100) at 4 K base temperature. For a laser excitation, we utilized nonresonant laser pumping at 532 nm in continuous wave mode. A laser spot size of
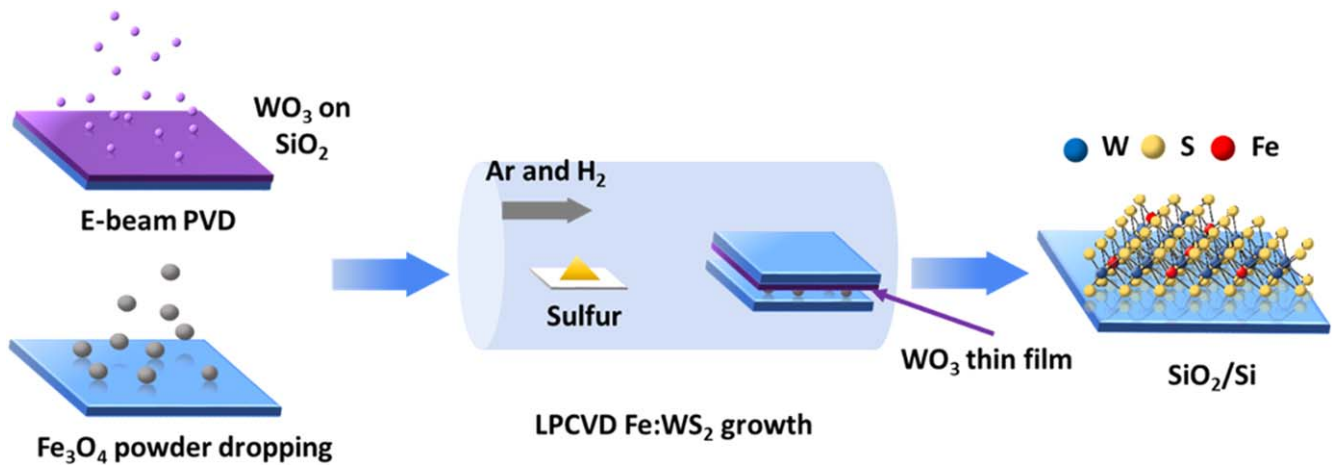
Figure 1. Schematic diagram of Fe:WS$_2$ growth process.

approximately 0.85 microns was achieved using a cryogenic microscope objective lens with a numerical aperture of 0.82. The reflected PL signal was collected by the same objective and guided by a multi-mode fiber to a spectrometer with an attached liquid-nitrogen-cooled silicon charge-coupled device camera.

The XPS measurement was performed using a PHI VersaProbe III x-ray photoelectron spectroscopy (XPS) equipped with a monochromatic Al Kα source ($\lambda = 1486.7$ eV). For the calibration, the binding energy of the C1s peak was fitted to 284.8 eV. The spectral analysis software Multipeak was employed for XPS peak deconvolution, where Voigt line shape and an active Shirley background were used for peak fitting.

Magnetic measurements were performed using a Superconducting Quantum interference Device Magnetometer (Quantum Design Model 2000) with the magnetic field applied parallel to the substrate plane. The magnetic field range was scanned from -2 to 2 T, while the temperature is maintained at 300 K. The large magnetic field range allowed the subtraction of the diamagnetic background signal of the substrate. Moreover, the temperature dependence measurement was performed from 300 to 400 K, while a magnetic field of 0.1 T was applied.

The PL emission of NV$^-$ center depends on the spin state of its ground state electron before excitation and is 20%–30% higher for $m_s = 0$ ('bright') sublevel than for the $m_s = \pm 1$ ('dark') sublevels [27]. This is because after excitation, decay through the intersystem crossing from the excited $m_s = \pm 1$ states make the relaxation partially non-radiative, decreasing the emitted fluorescence. Thus, the electron spin resonance (ESR) between the $m_s = 0$ and $m_s = \pm 1$ sublevels of the NV$^-$ center's ground state can be detected under optical excitation at 532 nm and a simultaneous microwave (MW) radiation at ~ 2.87 GHz polarizing these spin states. This resonance appears as a reduction of the detected fluorescence when a coupling (spin flipping) occurs between the bright state and the dark states by scanning the microwave frequency across the $m_s = 0 \rightarrow m_s = \pm 1$ transitions. Our NV$^-$ magnetometry experiments were conducted in a confocal microscopy setup. The samples were illuminated on the

surface using a frequency-doubled Nd:YAG laser (532 nm, 300 μW) focused with a NA $= 0.8$ objective giving a ~ 425 nm diffraction-limited spot size. Simultaneously, a sequence of 100 ms alternative on/off MW pulses (30 dBm before the antenna) was applied using a loop antenna centered about the focus, and their frequency was scanned across the resonance to polarize the electron spin of NV$^-$ centers. The PL signal of the NV$^-$ centers was then collected by the same objective and directed through a 550 nm long-pass filter into an avalanche photodiode. The relative PL is the ratio of total PL counts with and without MW radiation, where the resonance peaks appear at the frequencies of minimum ratio.

Projector augmented wave [28, 29] spin-polarized DFT [30, 31] calculations were carried out with the Vienna *ab initio* simulation package [32]. For this, the Perdew–Burke–Ernserhof generalized gradient approximation for the exchange-correlation functional [33] was used with a basis set including plane waves with energies less than or equal to 600 eV. The Brillouin zone of the pristine WS$_2$ unit cell was sampled with a $6 \times 6 \times 1$ Γ-centered Monkhorst-Pack grid [34]. Ionic relaxation iterations persisted until the Hellmann–Feynman forces on all atoms settled below 1 meV per Å, while electron field optimization iterations continued until changes in both the total energy and Kohn–Sham eigenvalues fell below 10^{-7} eV. For all structures, 20 Å of vacuum was inserted in the z-direction (out-of-plane direction) to negate interactions of each system with its periodic images. Larger Fe:WS$_2$ systems were simulated by substituting W atoms with Fe in a 5×5 supercell, and were sampled with a single k-point at Γ. To investigate whether or not these systems exhibit ferromagnetism, spin-polarized DFT calculations for each system were initialized with each atom possessing a magnetic moment of zero.

3. Results

3.1. Synthesis and characterizations of Fe:MoS$_2$ and Fe:WS$_2$ monolayers

Fe-doping of monolayer WS$_2$ (MoS$_2$) was realized by growing WS$_2$ (MoS$_2$) with Fe$_3$O$_4$ via LPCVD contact-growth
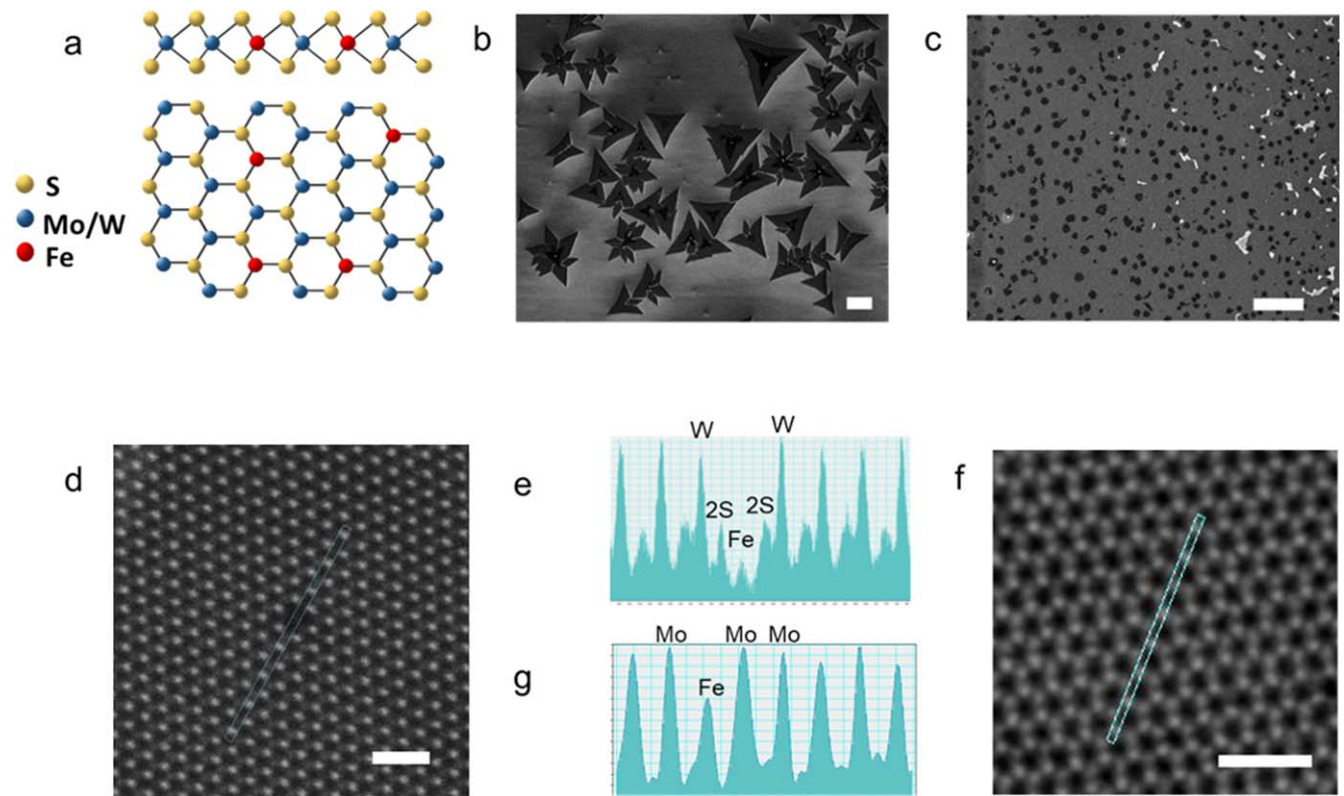
Figure 2. Schematic diagram, and SEM, and TEM images of Fe-doped MoS_2 and WS_2 monolayers. (a) Schematic of $Fe:MoS_2$ or $Fe:WS_2$ monolayers, (b) and (c) are SEM images of $Fe:WS_2$ and $Fe:MoS_2$. The scale bar is 5 μm. (d) and (f) are HAADF-STEM images of $Fe:WS_2$ and $Fe:MoS_2$ monolayers, respectively. The scale bar is 1 nm. (e) and (g) are STEM intensity profiles of $Fe:WS_2$ and $Fe:MoS_2$, respectively.

(see Methods section) [35]. Figure 2(a) depicts schematic top and side views of the atomic structures of $Fe:WS_2$ monolayers, where Fe atoms replace transition metal sites in the host lattice. Figures 2(b) and (c) show the scanning electron microscope (SEM) image, where the dark area represents a bilayer region and the bright spot is a Fe_3O_4 particle.

Figure 2(d) shows a HAADF-STEM image of a $Fe:WS_2$ monolayer. The brightness of atoms in STEM image is directly proportional to the square of atomic number ($\sim Z^2$), providing evidence to classify the atoms in 2D materials. The STEM intensity profile (figure 2(e)) clearly distinguishes atoms of W ($Z = 74$), 2S ($Z = 32$), and Fe ($Z = 26$). According to the intensity profile, the position of the Fe peak coincides with a W site, confirming the replacement of the transition metal (W) sites. Figures 2(f) and (g) show the STEM image and intensity profile of a $Fe:MoS_2$ monolayer confirming the substitution of Fe atoms in Mo sites. XPS was used to estimate the concentration of Fe atoms in $Fe:WS_2$ and $Fe:MoS_2$ monolayers, as shown in figures SI1(a) and (b) (available online at stacks.iop.org/NANO/32/095708/mmedia), which represent the XPS spectra of undoped/Fe-doped WS_2 monolayers and undoped/Fe-doped MoS_2 monolayers, respectively. The deconvolution of the spectra from Fe-doped samples yielded two peaks arising from Fe–O (blue) and Fe–S bonds (green) compared to the undoped cases. While the Fe–O peak is from unreacted Fe_3O_4 (powder) used as Fe source during the Fe-doping process, the Fe–S peak is correlated to substituted Fe atoms at transition metal sites of the monolayers

[36]. Using the Fe–S peak intensity, the Fe concentration was estimated to be approximately 0.6% for both Fe-doped samples. The AFM image of Fe:WS2 (figure SI2) shows that the doped sample is a monolayer.

3.2. Optical and Raman characterization

Figure 3(a) shows the PL spectra of $Fe:MoS_2$ (red curve) and undoped MoS_2 monolayers (black curve). The doped MoS_2 monolayers exhibit PL quenching by 35% and a redshift of 29 ± 0.5 meV when compared to the undoped case. This PL quenching arises from non-radiative channels activated by shallow traps within the MoS_2 bandgap when Fe dopants are introduced [37, 38]. Given that the charges are highly mobile and have access to a large amount of material in shallow trap states, it is expected that the MoS_2 sees more electron concentration when Fe dopants are introduced. Since Fe acts as an n-type dopant, the electron concentration in $Fe:MoS_2$ monolayers is expected to increase upon Fe-doping. Consequently, neutral excitons would be reduced along with an increase in negative trion emissions, causing a redshift in the PL peak position, which is consistent with previous studies [39, 40]. Figure 3(b) shows the PL spectra of $Fe:WS_2$ (red curve) and undoped WS_2 monolayers (back curve). Interestingly, we find that $Fe:WS_2$ shows the blue shift of the PL peak position by 13 ± 0.5 meV (and 40% quenching) compared to the undoped case. This blue-shift can be attributed to Fe dopants in WS_2 monolayers, which produce deep-level defects (rather than shallow trap states) [41]. Given that deep
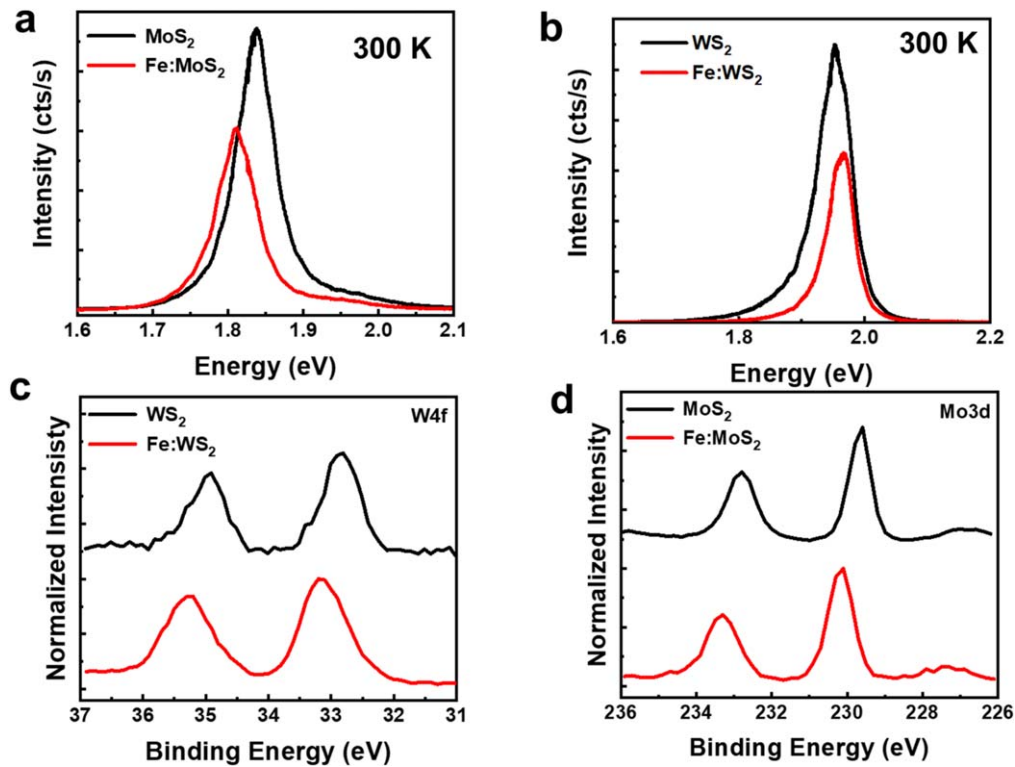
Figure 3. PL and XPS data of Fe-doped and undoped MoS_2 and WS_2 monolayers. (a) PL spectra of Fe:MoS_2 and MoS_2 monolayers at 300 K. The Fe:MoS_2 peak is red-shifted. (b) PL spectra of Fe:WS_2 and WS_2 monolayers at 300 K. The Fe:WS_2 peak is slightly blue-shifted. (c) XPS spectra of Fe:WS_2 and WS_2 monolayers. The blue-shift of binding energies of W in Fe:MoS_2 indicates that the Fe is an n-type dopant. (D) XPS spectra of Fe:MoS_2 and MoS_2 monolayers. The blue-shift of W peaks in Fe:MoS_2 also shows the Fe is an n-type dopant.

trap states are deeply localized charge states in the bandgap of the material, and the charges are immobile in them, the charge concentrations are only available within a small region of the material, resulting in a decrease in the mobile electron concentration. Therefore, the negative trion intensity would be decreased, causing a blue-shifted in the PL peak position. Figures SI3(a) and (b) show the PL spectra at 4 K, where the A-exciton and the sulfur vacancy-induced emission become resolvable upon doping in MoS_2 with the intensity of the former dominating the intensity of the latter, unlike the case of Fe:WS_2. In addition, we find that while no doping-related linewidth broadening appears in MoS_2 case, WS_2 shows drastic PL broadening from 72 meV (WS_2) to 92 meV (Fe:WS_2) monolayers, providing another evidence that Fe: MoS2 monolayers possess different dopant related trap states than Fe:WS_2 [42].

It is generally recognized that in semiconductors, Raman modes are sensitive to a perturbation such as doping due to the changes in material's electronic band structure caused by doping [27]. Substitutional doping of TMDs affects the $A_1^{'}$ vibrational mode (the out-of-plane vibration of chalcogen atoms) due to the change in electron density, consequently altering the strength of electron-phonon couplings in TMDs [43]. Since changes in electron density of shallow and deep trap state are different, we examined the changes in phonon frequency of both undoped and Fe-doped WS_2 and MoS_2 monolayers using Raman spectroscopy. Figure SI4(a) shows the Raman spectra of both Fe:MoS_2 (red curve) and pristine

MoS_2 (black curve) monolayers. The $A_1^{'}$ mode of the Fe:MoS_2 monolayers shifts to higher wavenumbers compared to the undoped monolayers, indicating that the $A_1^{'}$ mode is sensitive to doping. The redshift of $A_1^{'}$ mode is attributed to the increased electron density of the layer, supporting that the Fe impurity is an n-type dopant, which is consistent with an earlier study describing Raman spectra of n-type (Rhenium) Re:MoS_2 [24]. Substituting Fe dopants into TMDs causes $A_1^{'}$ mode linewidth broadening from 5.61 ± 0.3 to 6.82 ± 0.2 cm^{-1}, commensurate with recent studies of Fe:MoS_2 monolayers [25]. Figure SI4(b) shows the Raman spectra of Fe:WS_2 and undoped WS_2 monolayers, where no discernible $A_1^{'}$ mode peak shift and broadening were observed. However, we find an additional Raman vibrational mode at ~383 cm^{-1} in the Fe:WS_2 monolayers (figure SI4(c)), which is attributed to the substituted Fe atoms (i.e. FeS_2). The emergence of an additional Raman vibrational mode at 383 cm^{-1} with no apparent changes in the $A_1^{'}$ vibrational mode in Fe:WS_2 monolayers gives another indication that Fe:WS_2 monolayers have different Fe dopants-related trap states from Fe:MoS_2 monolayers.

3.3. Binding energy

Since the Fermi level can shift due to the concentration of charge and type of dopant carriers in doped semiconductors, an analysis of the Fermi level shift of TMDs can be used to investigate the change in electron density concentrations of
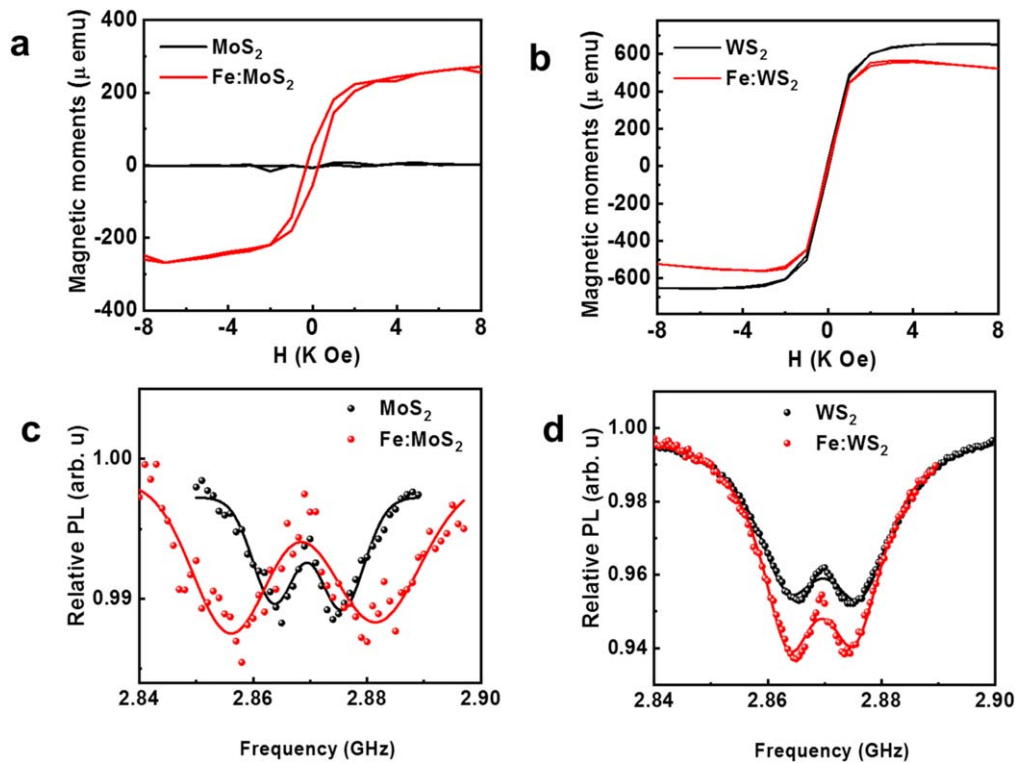
Figure 4. Magnetic characteristics of Fe-doped and undoped MoS_2 and WS_2 monolayers. (a)–(b) Magnetization *M–H* curves of doped and undoped MoS_2 and WS_2 monolayers, respectively. A pronounced hysteresis loop is observed in MoS_2 monolayers upon Fe-doping, suggesting a magnetic phase transition to ferromagnetism. (c)–(d) Comparison of ODMR spectra of NV^- centers coated on Fe-doped and undoped MoS_2 and WS_2 monolayers, respectively. The resonance dips for the case of $Fe:MoS_2$ display apparent Zeeman shifts revealing the local magnetic field. No discernible shifts were observed for the case of $Fe:WS_2$. All data were recorded at RT.

TMDs upon Fe substitutional doping. Figure 3(c) shows the XPS spectra of W in the $Fe:WS_2$ monolayers (red curve). For comparison, we also measured the XPS spectra of undoped WS_2 monolayers (black curve). The binding energy of $W4f_{5/2}$ (at 35.2 eV) and $W4f_{7/2}$ (at 33.2 eV) from the $Fe:WS_2$ monolayers are ∼0.25 eV higher than those from undoped WS_2 monolayers. This result implies that the Fermi energy of $Fe:WS_2$ monolayers is higher than that of the undoped ones, indicating that Fe is an n-type dopant, which is consistent with an earlier study [44]. Similarly, figure 3(d) shows the XPS spectra of Mo in the $Fe:MoS_2$ (red line) and undoped MoS_2 monolayers (black line), respectively. The binding energies of $Mo3d_{3/2}$ (233.3 eV) and $Mo3d_{5/2}$ (230.1 eV) in the $Fe:MoS_2$ is ∼0.5 eV higher than those of undoped MoS_2 monolayers. Since, in shallow trap states, more electrons are available than deep trap states, this result explains the twice as much blue-shifted binding energy of $Fe:MoS_2$ compared to that of $Fe:WS_2$ as more electrons are available in $Fe:MoS_2$ than $Fe:WS_2$ monolayers.

3.4. Magnetic characterization

To study the impact of Fe dopants on the magnetic properties of WS_2 and MoS_2, we measured the magnetization *M–H* curves of undoped and Fe-doped monolayers via a SQUID magnetometer. Figure 4(a) shows that $Fe:MoS_2$ monolayers exhibit a magnetic phase transition to ferromagnetism, as evidenced by observing a *M–H* hysteresis loop. It is worth

mentioning that the magnetization *M–H* curves are obtained after subtraction of a well-known linear diamagnetic background, which is common in the TMDs semiconductors [16]. One should note that the background affects only the *y*-axis and does not produce a shift on the *x*-axis. Figure 4(b) shows magnetization data of WS_2 and $Fe:WS_2$ monolayers, which does not show a measurable magnetic phase transition. The absence of ferromagnetism in $Fe:WS_2$ may arise from inadequate concentrations of Fe dopants or the presence of paired Fe atoms with the zero-net magnetic moments in $Fe:WS_2$.

To further investigate the magnetic features of our Fe-doped monolayers, we also performed spatially resolved magnetometry using NV^- centers in nanodiamonds. Given that the electron spin energy levels of NV^- centers are ultrasensitive to local magnetic fields induced by ferromagnet atoms, performing magnetometry based on the optically detected magnetic resonance (ODMR) in these spin states can give insight into local magnetic properties of our Fe-doped monolayers. The defect (color) center in diamond is generally recognized as a promising platform for various applications in quantum sensing [45], nanoscale metrology [46, 47], and quantum information processing [48]. While the ODMR-based magnetometry is extendible to cryogenic temperatures by conducting the experiments in a cryostat, we performed our measurements at RT only. The ESR signal of NV^- centers can split into a pair of dips when the degeneracy of the $m_s = \pm 1$ sublevels is lifted by an external magnetic field (see Methods section). We analyzed the net Zeeman shifts in the ESR dips of NV^- centers in
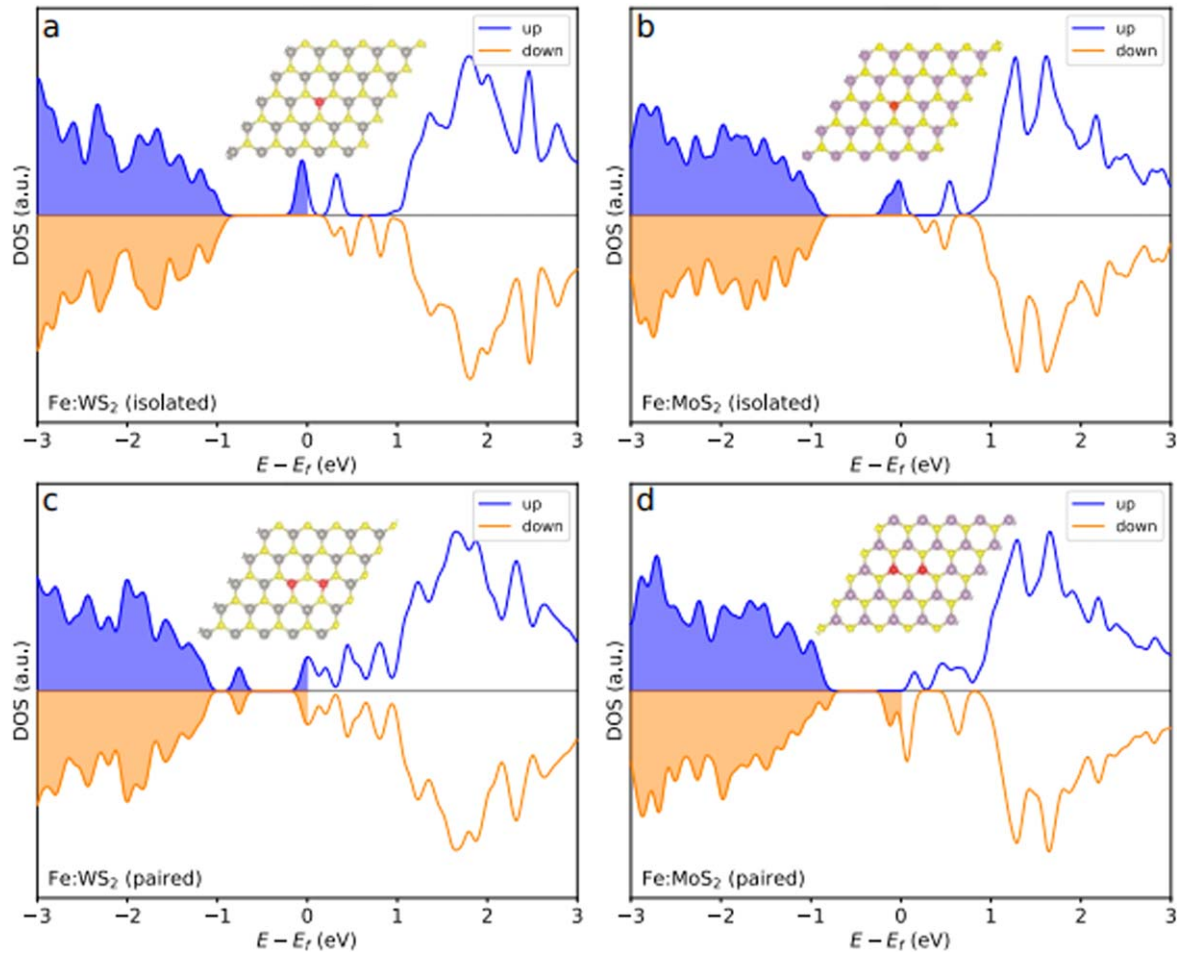
Figure 5. DFT calculations of Fe:MoS$_2$ and Fe:WS$_2$ monolayers. Spin-polarized density of states for isolated Fe dopants in (a) Fe:WS$_2$ and (b) Fe:MoS$_2$ and paired Fe dopants in (c) Fe:WS$_2$ and (d) Fe:MoS$_2$. The filled regions denote occupied states.

a spin-coat proximity [49] of our materials to measure any local magnetic field induced by the Fe dopants. Figures 4(c) and (d) show a comparison of exemplary ODMR signals of NV$^-$ centers in the vicinity of Fe-doped and undoped MoS$_2$ and WS$_2$ monolayers. The ∼10 MHz energy splitting between the ESR dips for the undoped cases in both panels shows a readily broken degeneracy of $m_s = \pm 1$ sublevels due to a pseudo-magnetic field caused by non-axial strain in the nanodiamond crystals. We subtracted this splitting from the total to find out the net Zeeman shifts due to any local magnetic field induced by the Fe dopants in the monolayers. Figure 4(c) shows an apparent net energy splitting for the case of Fe-doped MoS$_2$ compared to the undoped area of the same sample. We performed a statistical analysis (not shown) on the net shifts at 4×5 spots of a 20 μm $\times$ 25 μm grid on each area which resulted in a mean net splitting (∼11 MHz) only at the Fe:MoS$_2$ area. According to the Zeeman splitting term in the NV$^-$ center's spin Hamiltonian [46] $\Delta E = g_e \mu_B \mathbf{B}.\hat{S}$, with g_e and μ_B being the Landé g-factor and Bohr magneton respectively, this energy shift yields an average projection of a 0.5 ± 0.1 mT local magnetic field on the NV$^-$ centers' spin. This reveals an apparent preserved magnetization induced on this sample upon Fe-doping and is an indication of RT ferromagnetism of Fe:MoS$_2$ monolayers. In contrast, performing

similar experimental procedure on Fe-doped and undoped areas of WS$_2$ showed no discernible shifts in the ESR dips (see figure 4(d) for an illustrative comparison). The fact that Fe-doped area of WS$_2$ shows no local magnetic strength long after loading indicates that this monolayer does not possess a pre-served magnetization. In order to examine the ability of Fe:WS$_2$ to maintain magnetization in short-term, we performed ODMR measurements immediately after applying a short (100 ms) pulse of magnetic field (100 mT) at each step of the MW frequency scan. The results still showed no noticeable shifts in the ESR dips, ruling out the ferromagnetism of Fe:WS$_2$ and suggesting a zero net magnetic moment caused by an equal number of opposite Fe electron spins.

3.5. DFT modeling

To understand why ferromagnetism is not observed in Fe:WS$_2$, spin-polarized DFT was used to simulate WS$_2$ with substitutional Fe dopants. These calculations can predict ferromagnetism in the material if the ground state occupation of one spin projection is greater than the other. First, isolated Fe dopants were simulated by replacing a single W atom with Fe in a 5×5 WS$_2$ supercell. The resulting density of spin states, shown in figure 5(a), depicts that there are more

Table 1. Charge transfers to and magnetic moments of Fe atoms in Fe:WS$_2$ and Fe:MoS$_2$. The paired row shows the charge transfers to and magnetic moments of both Fe atoms in their respective systems.

	Charge-transfer (e^-)		Magnetic moment (μ_B)	
	Fe:WS$_2$	Fe:MoS$_2$	Fe:WS$_2$	Fe:MoS$_2$
Isolated	0.733	0.716	1.179	1.176
Paired	0.667, 0.668	0.713, 0.797	0.000, 0.000	1.165, 2.071

spin-up than spin-down states below the Fermi-level, signifying that the system is ferromagnetic. However, when Fe dopant atoms are paired, so that two adjacent W sites are replaced with Fe, the density of spin-up and spin-down states are identical (figure 5(c)), suggesting that Fe:WS$_2$ is paramagnetic when Fe atoms occupy adjacent sites. This behavior differs from that of Fe:MoS$_2$, which exhibits ferromagnetic behavior for both isolated and paired Fe dopant configurations, as shown in figures 5(b) and (d). Paired Fe atoms induce more structural distortion in Fe:WS$_2$ than in Fe:MoS$_2$. This distortion pulls the Fe atoms apart, giving them more room to accumulate electric charge (see figure SI5). This could explain why more charge is transferred away from paired Fe atoms in Fe:WS$_2$ than in Fe:MoS$_2$. Meanwhile, isolated Fe atoms do not distort the TMD structures, so the Fe atoms host similar amounts of charge in both TMDs (figure SI5).

We furthermore investigated the origin of the difference in these magnetic behaviors by examining the amount of charge transfer between the Fe dopants and neighboring S atoms. As S is more electronegative than Fe, S is expected to pull negative charge from the valence states of neighboring Fe. Doing so can unpair a d-orbital electron bound to a Fe atom, granting it a net magnetic moment. We used a Bader charge analysis [50–52] to investigate the degree of this charge transfer in all Fe-doped systems considered. Table 1 shows that the charge transfer to isolated Fe is very similar in Fe:WS$_2$ and Fe:MoS$_2$. Correspondingly, the isolated Fe atoms have a similar nonzero magnetic moment. However, when Fe is paired, the charge transfer to the Fe atoms in Fe:WS$_2$ is notably smaller than those in Fe:MoS$_2$. This phenomenon could explain why the Fe atoms in Fe:WS$_2$ lack a magnetic moment. Furthermore, the charge transfer to paired Fe atoms in Fe:MoS$_2$ is not equal, and the Fe atom that has gained more charge also nets a larger magnetic moment.

Recalculating the magnetic moments using LDA + U yielded results similar to those of PBE (see table SI1). The most notable difference is that LDA + U predicts that paired Fe atoms have small but nonzero magnetic moments in Fe:WS$_2$, while PBE predicts that their magnetic moments vanish. However, these magnetic moments are sensitive to the difference between the Hubbard term U and the exchange term J [53], and determining the appropriate values of U and J is beyond the scope of this work. Here, we used $U = 1$ and $J = 1$. Regardless, both PBE and LDA + U predict that the magnetic moments of paired Fe atoms are weaker in Fe:WS$_2$

than in Fe:MoS$_2$, which is consistent with our experimental findings (table SI1).

4. Conclusions

We have studied the effects of Fe-doping on the magnetic and optical properties of *in situ* synthesized Fe:WS$_2$ and Fe:MoS$_2$ monolayers. The presence of Fe atoms in transition metal sites (Mo or W) was confirmed using the HAADF-STEM intensity profile. While both Fe:MoS$_2$ and Fe:WS$_2$ were found to be n-type materials, a new Raman peak around 383 cm^{-1} was found only in Fe:WS$_2$ monolayers, which is another evidence of Fe-doping. The PL spectra of Fe:MoS$_2$ (Fe:WS$_2$) is redshifted (blue-shifted), while they are all quenched. Importantly, The SQUID result indicates that Fe:WS$_2$ monolayers are paramagnetic, while Fe:MoS$_2$ monolayers remain ferromagnetic at RT. The ODMR-based magnetometer with NV-center confirmed that Fe:MoS$_2$ is ferromagnetic while Fe:WS$_2$ is paramagnetic. The ODMR spectrum showed the energy splitting between the two typical ESR dips of the NV centers to be ∼21 MHz in the vicinity of Fe:MoS$_2$ monolayers. This splitting was significantly larger than the splitting for undoped MoS$_2$, demonstrating the presence of a local magnetic field in Fe:MoS$_2$ monolayers. However, no enhancement in the energy splitting between two ESR dips of Fe:WS$_2$ and WS$_2$ monolayers was observed, indicating that there was no long-range order ferromagnetic states in Fe:WS2. The DFT calculations were consistent with the experimental observations. The results from DFT calculation considering PBE approximation indicate that the observed properties are likely to arise from charge transfer between the Fe dopants and neighboring S atoms, depending on the structure of the doped system. While isolated Fe atoms induce similar ferromagnetic behaviors in both MoS$_2$ and Fe:WS$_2$, the magnetic moments of paired Fe atoms vanish only in Fe:WS$_2$, which explains different magnetic properties between Fe:WS$_2$ (paramagnetic) and Fe:MoS$_2$ (ferromagnetic). Furthermore, LAD + U considered DFT calculation showed weaker magnetic moments of paired Fe atoms in Fe:WS2 than in Fe:MoS2. Given that the magnetic moments are depending on the difference between the Hubbard term and the exchange term, all the experimental and theoretical results are consistent. These contrasting magnetic behaviors caused by paired Fe atoms can be attributed to paired Fe atoms generating more accumulated electric charge in Fe:WS2 by pulling the Fe atoms apart. These findings allow us to control the material's magnetic properties layer-by-layer and can be applied for spintronics.

ORCID iDs

Kamran Shayan https://orcid.org/0000-0003-0476-1328
Siamak Dadras https://orcid.org/0000-0003-4994-761X
Vincent Meunier https://orcid.org/0000-0002-7013-179X
Eui-Hyeok Yang https://orcid.org/0000-0003-4893-1691

References

[1] Ohno H, Munekata H, Penney T, von Molnár S and Chang L L 1992 Magnetotransport properties of p-type (In,Mn)As diluted magnetic III-V semiconductors *Phys. Rev. Lett.* **68** 2664–7

[2] Ohno H, Shen A, Matsukura F, Oiwa A, Endo A, Katsumoto S and Iye Y 1996 (Ga,Mn)As: a new diluted magnetic semiconductor based on GaAs *Appl. Phys. Lett.* **69** 363–5

[3] Reed M L J, El-Masry N A, Stadelmaier H H, Ritums M K, Reed M L J, Parker C A, Roberts J C and Bedair S M 2001 Room temperature ferromagnetic properties of (Ga, Mn)N *Appl. Phys. Lett.* **79** 3473–5

[4] Yan W, Sun Z, Liu Q, Li Z, Pan Z, Wang J, Wei S, Wang D, Zhou Y and Zhang X 2007 Zn vacancy induced room-temperature ferromagnetism in Mn-doped ZnO *Appl. Phys. Lett.* **91** 062113

[5] Dietl T 2010 A ten-year perspective on dilute magnetic semiconductors and oxides *Nat. Mater.* **9** 965–74

[6] Matsukura F, Ohno H, Shen A and Sugawara Y 1998 Transport properties and origin of ferromagnetism in (Ga, Mn)As *Phys. Rev. B* **57** R2037–40

[7] Huang B *et al* 2017 Layer-dependent ferromagnetism in a van der Waals crystal down to the monolayer limit *Nature* **546** 270–3

[8] Kim M *et al* 2019 Micromagnetometry of two-dimensional ferromagnets *Nat. Electron.* **2** 457–63

[9] Gong C *et al* 2017 Discovery of intrinsic ferromagnetism in two-dimensional van der Waals crystals *Nature* **546** 265–9

[10] Deng Y *et al* 2018 Gate-tunable room-temperature ferromagnetism in two-dimensional Fe3GeTe2 *Nature* **563** 94–9

[11] Fei Z *et al* 2018 Two-dimensional itinerant ferromagnetism in atomically thin Fe3GeTe2 *Nat. Mater.* **17** 778–82

[12] Lin G T *et al* 2017 Tricritical behavior of the two-dimensional intrinsically ferromagnetic semiconductor CrGeTe3 *Phys. Rev. B* **95** 245212

[13] Fan X L, An Y R and Guo W J 2016 Ferromagnetism in transitional metal-doped MoS$_2$ monolayer *Nanoscale Res. Lett.* **11** 154

[14] Mishra R, Zhou W, Pennycook S J, Pantelides S T and Idrobo J-C 2013 Long-range ferromagnetic ordering in manganese-doped two-dimensional dichalcogenides *Phys. Rev. B* **88** 144409

[15] Lin X and Ni J 2014 Charge and magnetic states of Mn-, Fe-, and Co-doped monolayer MoS$_2$ *J. Appl. Phys.* **116** 044311

[16] Tongay S, Varnoosfaderani S S, Appleton B R, Wu J and Hebard A F 2012 Magnetic properties of MoS$_2$: existence of ferromagnetism *Appl. Phys. Lett.* **101** 123105

[17] Ahmed S *et al* 2017 Inducing high coercivity in MoS$_2$ nanosheets by transition element doping *Chem. Mater.* **29** 9066–74

[18] Wang J, Sun F, Yang S, Li Y, Zhao C, Xu M, Zhang Y and Zeng H 2016 Robust ferromagnetism in Mn-doped MoS$_2$ nanostructures *Appl. Phys. Lett.* **109** 092401

[19] Ahmed S, Ding X, Murmu P P, Bao N N, Liu R, Kennedy J, Ding J and Yi J B 2018 Magnetic properties of Co doped WSe$_2$ by implantation *J. Alloys Compd.* **731** 25–31

[20] Ahmed S *et al* 2019 High coercivity and magnetization in WSe$_2$ by codoping Co and Nb *Small* **16** 1903173

[21] Martinez L M, Delgado J A, Saiz C L, Cosio A, Wu Y, Villagrán D, Gandha K, Karthik C, Nlebedim I C and Singamaneni S R 2018 Magnetic and electrocatalytic properties of transition metal doped MoS$_2$ nanocrystals *J. Appl. Phys.* **124** 153903

[22] Habib M, Muhammad Z, Khan R, Wu C, Ur Rehman Z, Zhou Y, Liu H and Song L 2018 Ferromagnetism in CVT grown tungsten diselenide single crystals with nickel doping *Nanotechnology* **29** 15701

[23] Xia B, Guo Q, Gao D, Shi S and Tao K 2016 High temperature ferromagnetism in Cu-doped MoS$_2$ nanosheets *J. Phys. D: Appl. Phys.* **49** 165003

[24] Kochat V *et al* 2017 Re doping in 2D transition metal dichalcogenides as a new route to tailor structural phases and induced magnetism *Adv. Mater.* **29** 1703754

[25] Fu S *et al* 2020 Enabling room temperature ferromagnetism in monolayer MoS$_2$ via *in situ* iron-doping *Nat. Commun.* **11** 2034

[26] Yun S J, Duong D L, Ha D M, Singh K, Phan T L, Choi W, Kim Y and Lee Y H 2020 Ferromagnetic order at room temperature in monolayer WSe$_2$ semiconductor via vanadium dopant *Adv. Sci.* **7** 1903076

[27] Harima H 2004 Raman studies on spintronics materials based on wide bandgap semiconductors *J. Phys. Condens. Matter* **16** S5653–60

[28] Blöchl P E 1994 Projector augmented-wave method *Phys. Rev. B* **50** 17953–79

[29] Kresse G and Joubert D 1999 From ultrasoft pseudopotentials to the projector augmented-wave method *Phys. Rev. B* **59** 1758–75

[30] Hohenberg P and Kohn W 1964 Inhomogeneous electron gas *Phys. Rev.* **136** B864–71

[31] Kohn W and Sham L J 1965 Self-consistent equations including exchange and correlation effects *Phys. Rev.* **140** A1133–8

[32] Kresse G and Furthmüller J 1996 Efficiency of *ab-initio* total energy calculations for metals and semiconductors using a plane-wave basis set *Comput. Mater. Sci.* **6** 15–50

[33] Perdew J P, Burke K and Ernzerhof M 1996 Generalized gradient approximation made simple *Phys. Rev. Lett.* **77** 3865–8

[34] Monkhorst H J and Pack J D 1976 Special points for Brillouin-zone integrations *Phys. Rev.* B **13** 5188–92

[35] Kang K, Godin K and Yang E H 2015 The growth scale and kinetics of WS$_2$ monolayers under varying H2 concentration *Sci. Rep.* **5** 13205

[36] Li B, Xing T, Zhong M, Huang L, Lei N, Zhang J, Li J and Wei Z 2017 A two-dimensional Fe-doped SnS2 magnetic semiconductor *Nat. Commun.* **8** 1–7

[37] Zhang S, Hill H M, Moudgil K, Richter C A, Hight Walker A R, Barlow S, Marder S R, Hacker C A and Pookpanratana S J 2018 Controllable, wide-ranging n-Doping and p-doping of monolayer group 6 transition-metal disulfides and diselenides *Adv. Mater.* **30** 04EH07

[38] Wang S Y *et al* 2014 Optical and electrical properties of MoS$_2$ and Fe-doped MoS$_2$ *Jpn. J. Appl. Phys.* **53** 04EH07

[39] Mouri S, Miyauchi Y and Matsuda K 2013 Tunable photoluminescence of monolayer MoS$_2$ via chemical doping —supporting info *Nano Lett.* **13** 5944–8

[40] Li L and Carter E A 2019 Defect-mediated charge-carrier trapping and nonradiative recombination in WSe$_2$ monolayers *J. Am. Chem. Soc.* **141** 10451–61

[41] Peimyoo N, Shang J, Cong C, Shen X, Wu X, Yeow E K L and Yu T 2013 Nonblinking, intense two-dimensional light emitter: monolayer WS$_2$ triangles *ACS Nano* **7** 10985–94

[42] Moody G *et al* 2015 Intrinsic homogeneous linewidth and broadening mechanisms of excitons in monolayer transition metal dichalcogenides *Nat. Commun.* **6** 8315

[43] Iqbal M W, Shahzad K, Akbar R and Hussain G 2020 A review on Raman finger prints of doping and strain effect in TMDCs *Microelectron. Eng.* **219** 111152

[44] Tedstone A A, Lewis D J and O'Brien P 2016 Synthesis, properties, and applications of transition metal-doped layered transition metal dichalcogenides *Chem. Mater.* **28** 1965–74

[45] Schirhagl R, Chang K, Loretz M and Degen C L 2014 Nitrogen-vacancy centers in diamond: nanoscale sensors for physics and biology *Annu. Rev. Phys. Chem.* **65** 83–105

[46] Rondin L, Tetienne J-P, Hingant T, Roch J-F, Maletinsky P and Jacques V 2014 Magnetometry with nitrogen-vacancy defects in diamond *Rep. Prog. Phys.* **77** 056503

[47] Plakhotnik T, Doherty M W, Cole J H, Chapman R and Manson N B 2014 All-optical thermometry and thermal properties of the optically detected spin resonances of the NV—Center in Nanodiamond *Nano Lett.* **14** 4989–96

[48] Prawer S and Aharonovich I 2014 *Quantum Information Processing with Diamond : Principles and Applications* (Waltham, MA, USA: Woodhead Publishing)

[49] Shayan K, Liu N, Cupo A, Ma Y, Luo Y, Meunier V and Strauf S 2019 Magnetic proximity coupling of quantum emitters in WSe$_2$ to van der Waals Ferromagnets *Nano Lett.* **19** 7301–8

[50] Tang W, Sanville E and Henkelman G 2009 A grid-based Bader analysis algorithm without lattice bias *J. Phys. Condens. Matter* **21** 084204

[51] Sanville E, Kenny S D, Smith R and Henkelman G 2007 Improved grid-based algorithm for Bader charge allocation *J. Comput. Chem.* **28** 899–908

[52] Henkelman G, Arnaldsson A and Jónsson H 2006 A fast and robust algorithm for Bader decomposition of charge density *Comput. Mater. Sci.* **36** 354–60

[53] Nakamura H, Hayashi N, Nakai N, Okumura M and Machida M 2009 First-principle electronic structure calculations for magnetic moment in iron-based superconductors: an LSDA + negative U study *Physica* C **469** 908–11